



Antiparallel dimer structure of CELSR cadherin in solution revealed by high-speed-atomic force microscopy

Shigetaka Nishiguchi^{a,1} , Rinshi S. Kasai^{b,c,1} , and Takayuki Uchihashi^{a,d,e,1}

Edited by Barry Honig, Columbia University, New York, NY; received February 6, 2023; accepted April 3, 2023

Cadherin EGF LAG seven-pass G-type receptors (CELSR) cadherins, members of the cadherin superfamily, and adhesion G-protein-coupled receptors, play a vital role in cell–cell adhesion. The mutual binding of the extracellular domains (ectodomains) of CELSR cadherins between cells is crucial for tissue formation, including the establishment of planar cell polarity, which directs the proper patterning of cells. CELSR cadherins possess nine cadherin ectodomains (EC1–EC9) and noncadherin ectodomains. However, the structural and functional mechanisms of the binding mode of CELSR cadherins have not been determined. In this study, we investigated the binding mode of CELSR cadherins using single-molecule fluorescence microscopy, high-speed atomic force microscopy (HS-AFM), and bead aggregation assay. The fluorescence microscopy analysis results indicated that the *trans*-dimer of the CELSR cadherin constitutes the essential adhesive unit between cells. HS-AFM analysis and bead aggregation assay results demonstrated that EC1–EC8 entirely overlap and twist to form antiparallel dimer conformations and that the binding of EC1–EC4 is sufficient to sustain bead aggregation. The interaction mechanism of CELSR cadherin may elucidate the variation of the binding mechanism within the cadherin superfamily and physiological role of CELSR cadherins in relation to planar cell polarity.

cadherin | adhesion GPCR | HS-AFM

Cadherins are transmembrane proteins that rely on calcium to connect cells through the mutual binding of their extracellular domains (ectodomains) (1, 2). This mutual binding is essential for embryonic development and tissue formation, and defects in this process can cause severe diseases (3–5). Cadherins belong to a superfamily that is further divided into subgroups (6). Classical cadherins in vertebrates have been extensively studied; they have five tandem cadherin ectodomains (EC1–EC5), a single-pass transmembrane region, and a cytoplasmic domain that interacts with intracellular molecules. The binding of classical cadherins occurs through a domain-swapping mechanism where the membrane-distal EC1 of one cadherin swaps single or double tryptophan residues with the hydrophobic acceptor pocket of its partner's EC1, thereby creating a strand-swap dimer that allows for the connection of opposing cells in various tissues (1, 7–11). The insertion of calcium into the calcium-binding linker regions between each cadherin ectodomain is crucial for solidifying the rod-like shape of classical cadherins and forming the strand-swap dimer (12–14).

The *trans*-dimer formation (between opposing cells) via the membrane-distal tip interaction of the classical cadherin ectodomains is a well-documented binding mechanism (1, 7–14). In contrast, various binding modes have been reported for other cadherin subgroups. Clustered and nonclustered protocadherins, possessing six or seven cadherin ectodomains, respectively, form *trans*-dimers through the interaction of their membrane-distal four cadherin ectodomains (15–19). Their binding is critical for the formation of neuronal tissue, particularly the binding of clustered protocadherins, which contribute to neuronal self-avoidance (16–18). Furthermore, cadherin 23 and protocadherin 15, possessing 27 and 11 cadherin ectodomains, respectively, form a heterophilic *trans*-binding complex called a tip-link, functioning as mechano-transducers on hair cells in the inner ear (20–25). The tip-link cadherins (cadherin 23 and protocadherin 15) form linear *trans*-binding conformations in the large extracellular space on hair cells. Conversely, Fat and Dachshous cadherins, which possess a large number of cadherin ectodomains similar to those of the tip-link cadherins, tightly bend using the calcium-free linker regions, which lose their calcium-binding site between specific cadherin ectodomains and forms a heterophilic *trans*-dimer, to fit the large ectodomains in the narrow intercellular space of epithelial cells (26, 27). The structure and binding modes among cadherins are diverse; therefore, each subgroup has unique physiological functions in each subgroup.

Significance

Cadherin EGF LAG seven-pass G-type receptors (CELSR) cadherins, members of the cadherin superfamily defined by cadherin extracellular domains (ectodomains), and adhesion G-protein-coupled receptors, are necessary for cell–cell adhesion regarding polarity-dependent tissue formation. However, the structure and binding mechanism of CELSR cadherins are unknown. In this study, a combined analysis of single-molecule fluorescence microscopy, high-speed atomic force microscopy (HS-AFM), and bead aggregation assay showed that the *trans*-dimer of CELSR cadherin is a minimal adhesive unit between cells. Eight membrane-distal cadherin ectodomains of CELSR cadherin entirely overlapped by twisting to form antiparallel dimer conformations and four membrane-distal cadherin ectodomains are sufficient for *trans*-binding. This study provides insights into the structure and binding mechanism of CELSR cadherins and their functional implications.

Author contributions: S.N., R.S.K., and T.U. designed research; S.N. and R.S.K. performed research; S.N. and R.S.K. analyzed data; and S.N., R.S.K., and T.U. wrote the paper.

The authors declare no competing interest.

This article is a PNAS Direct Submission.

Copyright © 2023 the Author(s). Published by PNAS. This article is distributed under [Creative Commons Attribution-NonCommercial-NoDerivatives License 4.0 \(CC BY-NC-ND\)](https://creativecommons.org/licenses/by-nc-nd/4.0/).

¹To whom correspondence may be addressed. Email: shigetaka-nishiguchi@ims.ac.jp, rkasai@gifu-u.ac.jp, or uchihast@d.phys.nagoya-u.ac.jp.

This article contains supporting information online at <https://www.pnas.org/lookup/suppl/doi:10.1073/pnas.2302047120/-/DCSupplemental>.

Published April 24, 2023.

Cadherin EGF LAG seven-pass G-type receptors (CELSR) cadherins in vertebrates are homologous, referred to as Flamingo or Starry night, in flies (28–32). These seven-path transmembrane cadherins are classified within the adhesion G-protein-coupled receptors (GPCRs) (33). CELSR cadherins possess nine cadherin ectodomains (EC1–EC9), several noncadherin ectodomains (EGF-like, laminin G, hormone receptor, and GPCR proteolytic site domains), a seven-path transmembrane region, and a cytoplasmic domain (Fig. 1*A*). Three distinct CELSR cadherins (CELSR1, CELSR2, and CELSR3), exhibiting similar ectodomain organization, have been identified in mammals (28, 29, 34). The mutual binding of CELSR cadherins is crucial for the asymmetric recruitment of specific molecules at the cell–cell interface in planar cell polarity, which leads to proper cell patterning. This is necessary for the formation of cilia and regular and polarity-dependent tissues (32, 35–39). Cell aggregation assays and *ex vivo* analyses of brain slice cultures in previous studies show that cadherin ectodomains of CELSR2 can maintain cell aggregation and responsiveness of cell–cell contact for the upkeep of dendritic branches (40). However, fundamental structural information regarding the binding mode of CELSR cadherins is lacking (32, 34, 41). Structural analysis of CELSR cadherins may provide insight into the physiological roles and diversification of binding modes of cadherin superfamily. In this study, we utilized single-molecule fluorescence microscopy and high-speed atomic force microscopy (HS-AFM), as well as bead aggregation assay, to investigate the binding mode of human CELSR2. Single-molecule fluorescence microscopy showed that the *trans*-dimer is a minimal adhesive unit between cells. HS-AFM demonstrated that EC1–EC8 overlap entirely by twisting to form antiparallel dimer conformation. Additionally, the bead aggregation assay indicated that EC1–EC4 is sufficient to induce bead aggregation. The antiparallel dimer conformations observed by HS-AFM likely correspond to the *trans*-dimer of CELSR cadherins formed

between cells, based on observations through single-molecule fluorescence microscopy.

Results

Trans-Dimer of CELSR Cadherin as a Minimal Adhesive Unit between Cells Revealed by Single-Molecule Fluorescence Microscopy. First, we investigated the minimal adhesive unit of CELSR cadherin between cells using conventional and single-molecule fluorescence microscopy. Human CELSR2 was labeled using Halo on its C-terminal cytoplasmic end (CELSR2-Halo) and then exogenously expressed in mammalian cells (CHO cells). CHO cells expressing CELSR2-Halo were observed under conventional epi-fluorescence microscopy after 48 h of seeding on a glass-based dish. CELSR2-Halo fluorescence signals densely accumulated at the interface of two adjacent cells, suggesting that CELSR2 molecules contribute to cell–cell adhesion (Fig. 1*B* and *SI Appendix*, Fig. *S1 A and B*). The CELSR2 molecule fluorescence signal intensity at the cell–cell interface was 1.84 times higher than the simple sum of fluorescence signal intensities of two neighboring cells. These higher fluorescence signals suggest that the cell–cell interface between the two overlaying cells does not simply overlap but forms cell–cell junctions by accumulated CELSR2 molecules (*SI Appendix*, Fig. *S1 C and D*). To distinguish CELSR cadherins forming the *trans*-binding complex between cells at the single-molecule resolution on each cell, CELSR2 labeled with monomeric GFP on its cytoplasmic end (CELSR2-mGFP) was expressed in CHO cells and the cells expressing CELSR2-mGFP were mixed with cells expressing CELSR2-Halo before seeding for coculturing. After 48 h of seeding cocultured cells on a glass-based dish, single-molecule fluorescence microscopy was performed, revealing colocalization and codiffusion of single fluorescent spots of CELSR2-mGFP and CELSR2-Halo at the overlaying

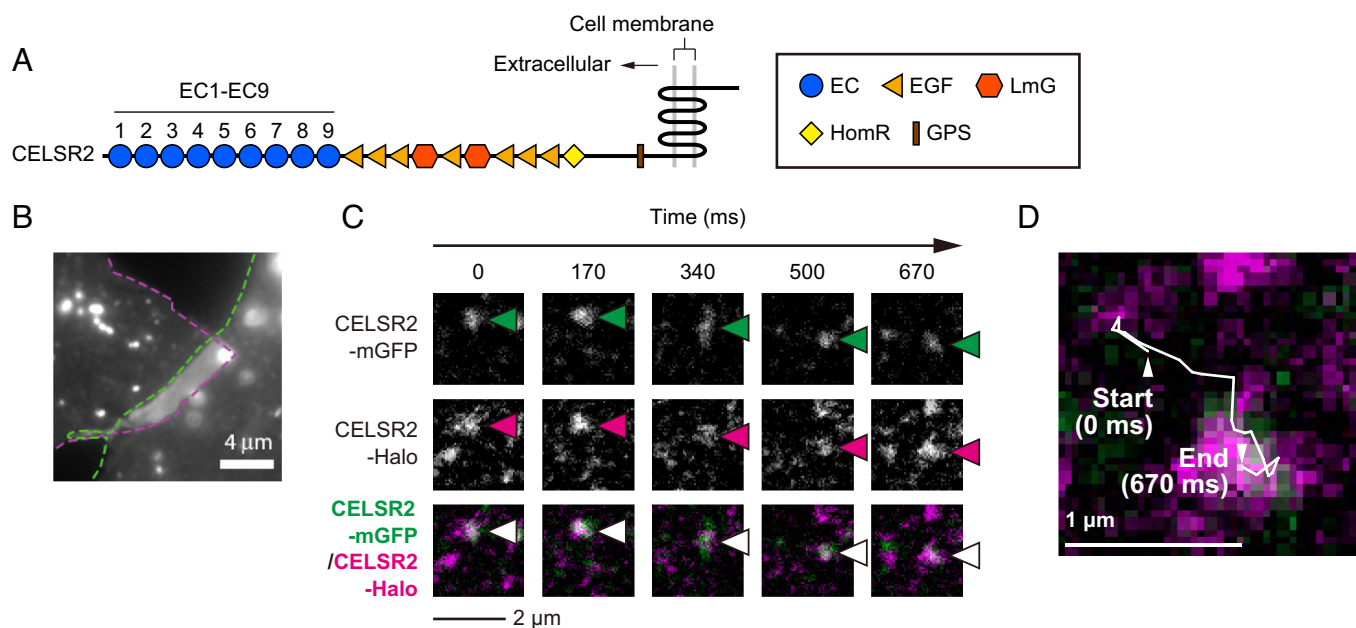


Fig. 1. Localization of CELSR cadherin at the interface of two adjacent cells according to fluorescence microscopy. (A) Schematic representation of the CELSR2 cadherin. EC, extracellular cadherin domain (cadherin ectodomain); EGF, EGF-like domain; LmG, laminin G domain; HomR, hormone receptor domain; GPS, GPCR proteolytic site domain. (B) Exogenous CELSR2-Halo accumulation at the interface of two adjacent CHO cells based on conventional epi-fluorescence microscopic observation, with the edges of two adjacent cells demarcated by green and magenta broken lines. Detailed information on the interface of two adjacent CHO cells is shown in *SI Appendix*, Fig. *S1*. (C) Colocalization and codiffusion of single fluorescence spots at the interface of two adjacent CHO cells exhibited exogenous CELSR2-mGFP and CELSR2-Halo as observed by single-molecule fluorescence microscopy, with green and magenta arrow heads pointing to CELSR2-mGFP and CELSR2-Halo, respectively. White arrowheads point to overlapping spots of CELSR2-mGFP and CELSR2-Halo. (D) The trajectory of codiffusing spots in C, with arrowheads at the start and end representing 0 ms and 670 ms in C, respectively. The trajectory was overlaid on the layered image of CELSR2-mGFP and CELSR2-Halo of 670 ms in C (*Bottom Right*). The layered image was trimmed and magnified from C. More examples of trajectories are included in *SI Appendix*, Fig. *S2*.

region of two adjacent cells (Fig. 1 *C* and *D*). Diffusion coefficients between codiffusion spots and noncodiffusion spots had no apparent difference; however, the codiffusions of CELSR2-mGFP and CELSR2-Halo were sustained above the $\sim 1\text{-}\mu\text{m}$ range and between 198 ms and 3,267 ms (Fig. 1*D* and *SI Appendix*, Figs. *S2* and *S3*). This long-time colocalization of diffusing spots up to 3,267 ms observed in this study was not observed in our previous observation of the incidental colocalization durations of less than 100 ms of fluorescent spots of representative G-protein-coupled receptors on the plasma membrane (42, 43). Moreover, the relative distances between these two spots were less than 200 nm over 88% of the time during codiffusion, showing the proximity of CELSR2-mGFP and CELSR2-Halo in long time durations at the cell–cell interfaces (*SI Appendix*, Fig. *S4*). These results suggest that *trans*-dimer is a minimal adhesive unit of CELSR cadherins between cells. However, accumulation of fluorescence signals of CELSR2-Halo observed by conventional epi-fluorescence microscopy indicates that the maturation of cell–cell adhesion may require more high-order complex, which is similar to those of previously reported cadherins (16, 23, 44). In addition, we confirmed the contribution of exogenously expressed CELSR2 for calcium-dependent cell–cell adhesion using CELSR2-Halo by cell aggregation assay (*SI Appendix*, Fig. *S5*).

Determination of Ectodomains Responsible for Binding of CELSR Cadherin by Bead Aggregation Assay. To determine ectodomains responsible for *trans*-binding of CELSR cadherin using bead

aggregation assay, we purified the full-length ectodomains of human CELSR2 (referred to as EX-full) from human cells (HEK293T cells) (Fig. 2*A* and *SI Appendix*, Fig. *S6*). First, we identified five amino acid residues from membrane-distal N terminus of purified proteins because the cDNA of CELSR2 cadherin used in this study contains prodomain and the furin protease cleavage recognition sequence before its EC1 (UniProtKB/Swiss-Prot: Q9HCU4). N-V-N-T-A (residues 174 to 178) was determined to be the N-terminal residues of the purified proteins. This N-terminal sequence indicated the removal of the prodomain by enzymatic cleavage at the furin protease cleavage recognition site during expression in HEK293T cells and that the EC1 is the N-terminal domain of the purified proteins. We then confirmed the calcium-dependent binding activity of the purified proteins using the bead aggregation assay (Fig. 2*A* and *B*). In addition, we prepared partial deletion constructs to narrow down the ectodomains from the membrane-proximal C-terminal regions. We then compared average areas of bead aggregation for EX-full and the deletion constructs, which is an assessment of the differences among the binding activities of different constructs and/or condition (Fig. 2*A* and *B* and *SI Appendix*, Fig. *S6*) (15, 45). The bead aggregation assay using the deletion constructs (referred to as EC1–8, EC1–7, EC1–6, EC1–5, EC1–4, EC1–3, EC1–2, and EC1, respectively, and the EC1–9 construct could not be purified owing to an unknown reason) revealed that the average areas of bead aggregation for EC1–8, EC1–7, EC1–6, and EC1–5 were similar or larger than that of EX-full (Fig. 2*C*). Furthermore, the average area of bead aggregation for EC1–4 in Ca^{2+} -containing

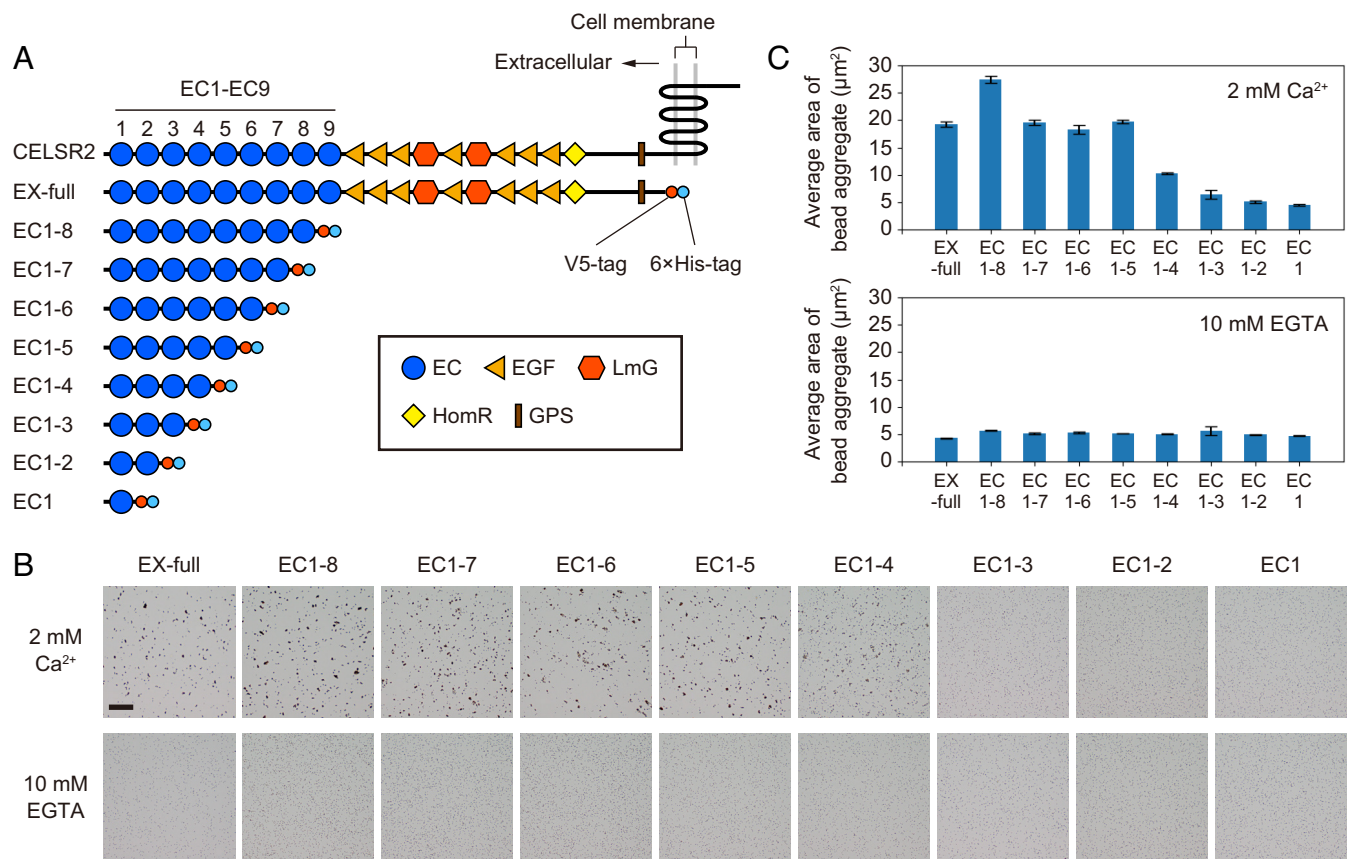


Fig. 2. Bead aggregation assay using full-length ectodomains of CELSR cadherin and its partial deletion constructs. (A) Schematic representation of the CELSR cadherin constructs used for bead aggregation assay. EC, extracellular cadherin domain (cadherin ectodomain); EGF, EGF-like domain; LmG, laminin G domain; HomR, hormone receptor domain; GPS, GPCR proteolytic site domain. All constructs contain V5-tag and His-tag on its membrane-proximal C-terminal side. (B) Representative images showing results of the bead aggregation assay in the presence of 2 mM Ca^{2+} (Upper images) or 10 mM EGTA (Lower images) using constructs in A. (Scale bar; 100 μm .) (C) Average area of bead aggregation calculated using images in B. Graph represents mean \pm SEM of average area of bead aggregation in four different images for each construct. Images represent two or more experiments. See also *SI Appendix*, Fig. *S7*.

buffer was approximately double in EGTA-containing buffer (and also beads without purified proteins in Ca^{2+} - or EGTA-containing buffer) (*SI Appendix, Fig. S7*). However, the area was approximately half of EX-full in the Ca^{2+} -containing buffer (Fig. 2C). In contrast, the average areas of bead aggregation of EC1–3, EC1–2, and EC1 were similar to that in the EGTA-containing buffer, indicating that these constructs had lost their calcium-dependent binding activity (Fig. 2C). These results suggest that the EC4 domain is required to induce bead aggregation; EC5 domain is also required for the complete calcium-dependent binding activity observed in EX-full (Fig. 2C).

HS-AFM Visualization of the Structures and Dynamics of CELSR Cadherin Ectodomains in Solution. Subsequently, we employed HS-AFM to observe EX-full molecules adsorbed on the mica surface in the same buffer solution (10 mM Hepes, 5 mM KCl, 140 mM NaCl, 2 mM CaCl_2 , pH 7.4) as the one used for the bead aggregation assay. The HS-AFM images indicated that EX-full molecules consist of strand-like and globule-like portions (Fig. 3A and *SI Appendix, Fig. S8*). The strand-like portion of the molecule displayed a hinge in the middle region and a bending motion at the hinge (Fig. 3A and B, *SI Appendix, Fig. S9*, and *Movie S1*). Angle distribution of the hinge of representative molecules ranged between 52° and 180° and flexibly changed the angle from the starting position during imaging (Fig. 3C and D). In addition, a dumbbell-like structure was observed, showing that the strand-like portions of protomers extensively overlap with antiparallel orientation (Fig. 3E and *SI Appendix, Fig. S8*). The dissociation of two protomers showed that the dumbbell-like structures are dimers and revealed a flexible

bending motion at the hinge of the strand-like portion in a single protomer, suggesting dimer conformation dissociation through the hinge of the strand-like portion (Fig. 3F, *SI Appendix, Fig. S10*, and *Movie S2*). Approximately 90% of EX-full molecules were observed as dumbbell-like dimer conformations, with the average length of the long axes calculated from individual dimers (-66.7 ± 0.4 nm; $n = 249$) exceeding those of classical cadherins (37.3 to 38.5 nm) (7, 44). Whereas most EX-full molecules formed dumbbell-like dimer conformations, we observed different conformations where the globule-like portions were in parallel contact, thus forming the dimers, trimers, and tetramers (Fig. 4A), and the dynamical dimerization processes through the globule-like portions (Fig. 4B and *Movie S3*). However, the population of the oligomers formed by the parallel contacts of the globule-like portions was less than ~5%.

To identify the membrane-distal and membrane-proximal sides of EX-full molecules observed by HS-AFM, we observed EX-full molecules in EGTA-containing buffer (*SI Appendix, Fig. S11*). Complete globular conformations which lose the strand-like portions suggested that the strand-like portions are formed by cadherin ectodomains which require calcium binding to linker regions of cadherin ectodomains to sustain the rod-like structure (12, 14). Furthermore, we observed EC1–8 consisting of eight membrane-distal cadherin ectodomains (Fig. 5A and B and *SI Appendix, Fig. S8*). The HS-AFM observation revealed that EC1–8 molecules primarily display a strand-like structure, supporting that the strand-like portion observed in EX-full molecules primarily represents membrane-distal cadherin ectodomains, whereas the globule-like portion is formed by membrane-proximal noncadherin ectodomains (Figs. 3 and 5 and *SI Appendix, Fig. S8*). Despite the resolution limitation of

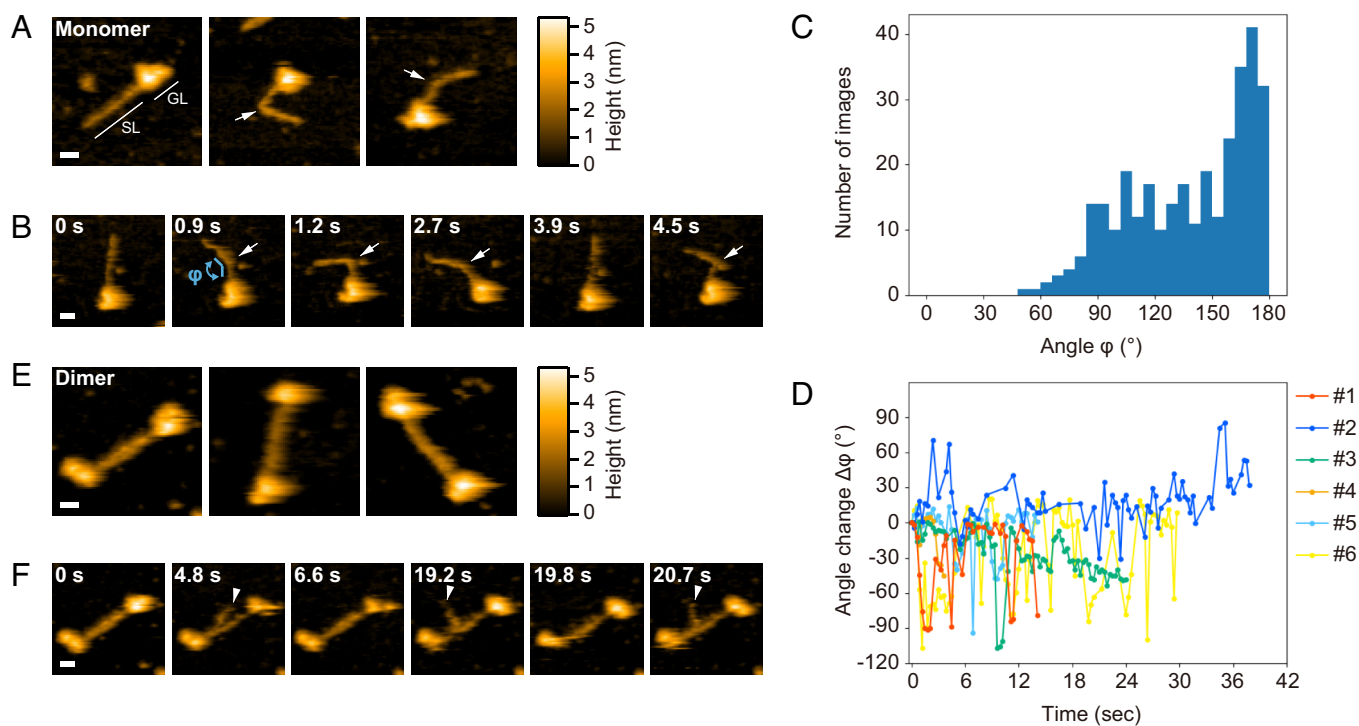


Fig. 3. HS-AFM visualization of full-length ectodomains of CELSR cadherin (EX-full) in solution. (A) Representative images of monomers. SL, strand-like portion; GL, globule-like portion. White arrows point to the single hinge region in strand-like portion. (B) Bending motion of monomer at the hinge region. “ ϕ ” represents the angles of the hinge region. Sequential images were captured at a scanning speed of 0.3 s/frame. (C) Histogram showing angle ϕ of the hinge region of sequential HS-AFM images of six representative monomers which display bending motion during imaging. In total, 318 images were analyzed. (D) Line graph showing angle change $\Delta\phi$ of the hinge region of the six monomers used in C. Six individual monomers were presented as #1 to #6. The data of #1 correspond with the monomer in B. Representative images of the molecules corresponding with #2 to #6 are shown in *SI Appendix, Fig. S9*. (E) Representative images of dimers formed by antiparallel overlapping between the strand-like portions. (F) Binding and unbinding of the strand-like portion of the single protomer in the antiparallel dimer conformations. White arrow head points to the tip portion of the single protomer. Sequential images were captured at a scanning speed of 0.3 s/frame. (Scale bars; 10 nm.) Images represent five experiments. More examples are presented in *SI Appendix, Figs. S8–S10*. See also *Movies S1* and *S2*.

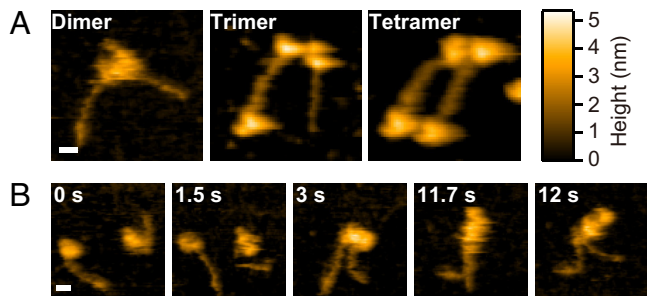


Fig. 4. Oligomers formed by globule-like portions of full-length ectodomains of CELSR cadherin (EX-full). (A) Representative images of dimers, trimers, and tetramers. (B) Dimer formation via globule-like portions. Sequential images were captured at a scanning speed of 0.3 s/frame. (Scale bars; 10 nm.) Images shown are representative of five experiments. See also [Movie S3](#).

HS-AFM precluding clear observation of protomers of EC1–8 dimers, the observed dissociation of the dimers suggests that the eight cadherin ectodomains are fully overlapped and entangled with protomers (Fig. 5*B* and [Movie S4](#)). The average length of the long axes of individual EC1–8 dimers (-39.1 ± 0.5 nm; $n = 81$) is close to that of the eight cadherin ectodomains (~ 36 nm) calculated from the dimension of single cadherin ectodomain (~ 4.5 nm) (7, 21). Considering the lateral tip convolution effect of AFM images, the actual length of the long axes of EC1–8 dimers may be shorter than depicted in the HS-AFM images, supporting the interpretation that EC1–EC8 overlap entirely (46). Additionally, we observed a shorter construct, EC1–5, because if EC1–EC8 domains entirely overlap by antiparallel orientation, free ectodomains in both sides of the dimer structure could be observed in shorter constructs. The HS-AFM observation of EC1–5 revealed that certain molecules displayed a straight structure that was shorter than that of EC1–8 molecules, while the other molecules displayed a globule structure (Fig. 5*C* and [SI Appendix, Fig. S8](#)). As expected, a part of the globule molecules had two free tails,

suggesting that the globule molecules are dimers (Fig. 5*C* and [SI Appendix, Fig. S8](#)). The globule structures of EC1–5 suggest that the dimer structures are formed by stacking protomers on the mica substrate and the dimer structures were not formed by flat contact between cadherin ectodomains but by entangling with protomers, indicating the possibility of the entangling structure suggested in EC1–8 dimers. Moreover, EC1–4 molecules also showed globular conformations. However, two free tails as seen in EC1–5 molecules could not be observed ([SI Appendix, Fig. S8](#)), suggesting that the orientation of EC1–4 molecules related to the mica substrate prevents detailed structural visualization. Nonetheless, the globular conformations may represent dimer conformations based on the observation of EC1–5 molecules. Therefore, further structural analysis using shorter constructs than EC1–5 could not be performed in this study.

Twisted Dimer Conformations of CELSR Cadherin Revealed by Localization Analysis of HS-AFM Images. To more clearly observe the configurations of EC1–8 dimers, we employed recently developed localization atomic force microscopy (LAFM) proposed by Heath et al. (47). This method enhances the resolution of HS-AFM images by identifying local maxima in the signals of individual pixels from multiple images of single molecules. To apply the LAFM analysis to the observation of CELSR cadherin, we treated the sample with 2% glutaraldehyde after the molecules were adsorbed on the mica surface to reduce the extensive dynamic motion of molecules and improve the resolution of HS-AFM images. The chemical fixation reduced the extensive dynamic motion of EC1–8 molecules, thus allowing us to record a number of high-resolution HS-AFM images from a single molecule to generate an LAFM image (Fig. 5*D* and *E*). General configurations of EC1–8 of HS-AFM images after the chemical fixation were similar to those observed without the fixation, suggesting that the fixation does not severely alter the nanometer scale-level conformation (Fig. 5*A*, *D*, and *E* and [SI Appendix, Figs. S8](#) and

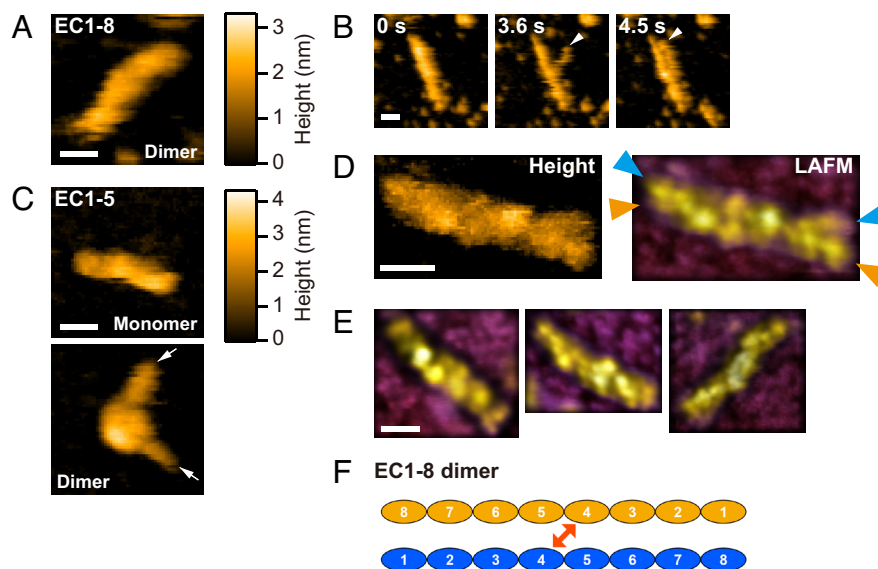


Fig. 5. Dimers of partial cadherin ectodomains of CELSR cadherin (EC1–8 and EC1–5). (A) A representative image of EC1–8 dimer. (B) Dissociation of dimer of EC1–8. White arrowhead points to the tip portion of single protomer. Sequential images were captured at a scanning speed of 0.3 s/frame. (C) Representative image of monomer and dimer of EC1–5. White arrows point to two tail portions of the dimer. (D) Representative raw image of dimer of EC1–8 in 2% GA (Left image). LAFM image generated by 30 images of single dimer in 2% GA (Right image). Blue and orange arrowheads point to the tip of each protomer. (E) Other representative LAFM images were generated using individual dimers of EC1–8 in 2% GA. 96, 112, and 28 images of single dimers were used for the LAFM images (Left image to Right image). (F) Schematic model of the protomers' orientation of EC1–8 dimer. The red two-direction arrow indicates EC4–EC4 interaction between protomers. (Scale bars; 10 nm.) Images shown are representative of two or more experiments. More examples are included in [SI Appendix, Figs. S8](#) and [S12](#). See also [Movie S4](#).

S12). Using a previously reported algorithm (47), we analyzed 28 to 112 images of individual single dimers of EC1–8 and generated the LAFM images. The LAFM analysis of EC1–8 showed that the protomers are fully overlapped with the twisted ectodomains (Fig. 5 *D* and *E*), indicating that the CELSR cadherins form antiparallel dimer conformations with fully overlapped and twisted EC1–EC8 between protomers.

Discussion

The structure and binding mechanism of CELSR cadherins have not been thoroughly examined owing to the challenges presented by their large ectodomains and variable conformations, thus complicating the utilization of averaging methods such as X-ray crystallography or single-particle analysis of electron microscopy. However, using techniques such as HS-AFM to visualize single-molecule structure and dynamics in solution, fluorescence microscopy, and bead aggregation assay, we elucidated the structure and binding mechanism of CELSR cadherins and its functional implication based on the structures discussed below.

Minimal Adhesive Unit between Cells and Essential Ectodomains for *Trans*-Binding. Conventional epi-fluorescence microscopic observations demonstrated that CELSR2 accumulates in areas of cell–cell contact. However, observations by single-molecule fluorescence microscopy revealed that the minimal adhesive unit of CELSR2 between cells is a *trans*-dimer, which is similar to those of classical cadherins reported in previous studies (Fig. 1) (48, 49). Although a previous study reported that cadherin ectodomains of CELSR2 were sufficient to form cell aggregation (40), our bead aggregation assay showed that EC1–4 retained calcium-dependent *trans*-binding activity and EC1–3 entirely lost this activity, suggesting that EC4 is an essential domain for the *trans*-binding of CELSR2 and potentially interacts with its counterpart (Fig. 2). In contrast, EC1–4 decreased the area of bead aggregation compared to that of EX-full, while the area of bead aggregation of EC1–5 was similar to that of EX-full, indicating that EC5 is necessary for the full activity of CELSR2 to form bead aggregation (Fig. 2). HS-AFM analysis revealed that CELSR2 forms an antiparallel dimer conformation by twisting EC1–EC8, which are fully overlapped between protomers; however, other cadherin ectodomains except for EC1–EC5 are not required to form bead aggregation similar to that observed in EX-full (Figs. 2 and 5 *D* and *E*). In this study, our bead aggregation assay did not assess the binding strength or affinity of each construct; therefore, we do not disregard the possible contribution of the other cadherin ectodomains to the binding of CELSR cadherins to a certain extent. Furthermore, the average area of bead aggregation of a part of the deletion constructs (e.g., EC1–8) was larger than that of EX-full, suggesting that the globule-like portions of noncadherin ectodomains observed by HS-AFM may cause steric effects to decrease the cadherin ectodomain binding affinity. However, further biophysical and structural analyses should be conducted in future studies to determine the precise contribution of each cadherin and noncadherin ectodomains to the CELSR cadherin binding.

Structure of Monomer and Dimer in Solution. The observation of EX-full and EC1–8 molecules using HS-AFM revealed that monomers of CELSR cadherin ectodomains could be structurally classified into strand-like and globule-like portions primarily composed of cadherin and noncadherin ectodomains, respectively (Fig. 3). Structural dynamics of EX-full demonstrated that the

strand-like portion consisting of cadherin ectodomains contains a single hinge region that can flexibly bend at variable angles (Fig. 3 *B–D*). CELSR cadherins possess a single Ca²⁺-free linker site between EC5 and EC6 (50), which corresponds to the location of the hinge region in the middle region of the strand-like portion of HS-AFM images; however, we were unable to directly confirm that the hinge region coincides with the border between EC5 and EC6 owing to resolution limitation of our HS-AFM. The flexible nature of the hinge region, which may correspond to the Ca²⁺-free linker site, is similar to that of previously reported *Drosophila* N-cadherin (51). In contrast, the single hinge region of the strand-like portion of protomers was not extensively kinked in the antiparallel dimer conformation (Fig. 3*E*). Furthermore, while most EX-full molecules formed antiparallel dimer conformations, dissociation and association of a single protomer with bending at the hinge region was observed, suggesting that the hinge region may contribute to the binding process (Fig. 3*F*). Localization analysis of HS-AFM images also showed that EC1–EC8 were fully overlapped between protomers in the dimer conformation (Fig. 5 *D* and *E*). This overlap suggests the possibility of EC4–EC4 interaction, confirming that EC4 is an essential domain for *trans*-binding to form bead aggregation (Fig. 5*F*). However, we could not determine specific domain pairs between protomers in the dimer conformation. The dimer conformations of EC1–5 molecules, which possess two free tails, confirmed the possibility of EC4–EC4 interactions based on the assumed orientation of EC1–8 dimer conformations (Fig. 5 *C* and *F*).

In contrast, the globule-like portion formed by noncadherin ectodomains was not necessary for the *trans*-binding of bead aggregation, and the results are consistent with most of the dimer conformations formed by strand-like portions of EX-full observed by HS-AFM (Figs. 2 and 3). The globule-like portion of noncadherin ectodomains observed in EX-full was similar to those of *Drosophila* E- and N-cadherin, which are classical cadherins, suggesting that the structure formed by a number of noncadherin ectodomains shares similar conformation among different cadherin subgroups (51). Most oligomers in EX-full exhibited antiparallel dimer conformations formed by the strand-like portion. However, dimer, trimer, and tetramer conformations were formed through parallel contact via the globule-like portions (Fig. 4), but the population of the oligomers formed by the parallel contact of the globule-like portions was less than ~5%. These findings suggest that the globule-like portions may serve as a *cis*-clustering interface borne by cadherin ectodomains in other cadherin subgroups; a similar interaction between noncadherin ectodomains has been observed in *Drosophila* E- and N-cadherin (51). Although we conducted LAFM analysis of the globule-like portions of EX-full molecules, the detailed structure of the globule-like portions could not be visualized primarily because of the irregular conformation, suggesting that some noncadherin ectodomains may not firmly interact with each other in the globular arrangement. Furthermore, previous mutational analysis of CELSR1 showed that mutation between EC7 and EC8 caused severe defects in tissue formation related to planar cell polarity (39). However, this mutation did not severely affect *trans*-binding activity but rather *cis*-interactions on the same cells. Our HS-AFM could not observe *cis*-like parallel interactions through the strand-like portions of cadherin ectodomains, suggesting that the mutation between EC7 and EC8 of CELSR1 may affect parallel interactions between globule-like portions of noncadherin ectodomains because the mutation is located near the membrane-proximal side of cadherin ectodomains. However, we cannot completely rule out the possibility of *cis*-interactions through the strand-like portions of CELSR cadherin ectodomains. Structural analyses using proteoliposomes or

tissue sections, as previously conducted in other cadherins, may facilitate further investigation of *cis*-interactions of CELSR cadherins (16, 23, 44, 52).

Difference between the *Trans*-Binding Mode of CELSR and Other Cadherins and Its Functional Implication. The antiparallel dimer conformation of CELSR cadherin observed by HS-AFM suggests that the conformation may represent the *trans*-binding mode between cells observed by single-fluorescence microscopy (Figs. 1C and 3E). The antiparallel overlapping of the EC1–EC8 domains of the CELSR cadherin dimer is in sharp contrast to tip interaction via the EC1 domain of vertebrate classical cadherin dimers (7, 11, 53). Conversely, previous studies have reported similar antiparallel dimer conformations formed by EC1–EC4 in clustered and nonclustered protocadherins (15, 16, 19). The overlapping of eight cadherin ectodomains of the CELSR cadherin dimer is the most extensive case of *trans*-dimer conformation in the cadherin superfamily reported. A notable characteristic of the antiparallel dimer of CELSR cadherin is its ~66.7 nm long axis in HS-AFM images which exceeds the 37.3 to 38.5 nm of classical cadherins estimated from X-ray crystallography (7, 44). However, colocalization of CELSR1 or Flamingo and classical cadherins in the cell–cell junctions of epithelial cells has been reported in previous studies (30, 37). The colocalization mechanism of CELSR cadherins and classical cadherins, which have different dimer sizes, is fascinating. In addition, recent studies have suggested that small extracellular vesicles (exosomes) containing Wnt proteins, which are the planar cell polarity pathway signaling ligands, diffuse in a polarity-dependent manner within the extracellular space (54, 55). Exosomes vary from 40 to 160 nm in diameter, and the large binding complex of CELSR cadherins, which is known to be a critical component of planar cell polarity, may locally serve as a physical spacer between cells to allow for specific exosome sizes (56). Further research is required to determine the contribution of the binding structure of CELSR cadherins in physiological contexts.

Summarily, a combined analysis of fluorescence microscopy, HS-AFM, and bead aggregation assay showed that the *trans*-dimer of CELSR cadherin is a minimal adhesive unit between cells, EC1–EC8 of CELSR cadherin fully overlapped by twisting to form antiparallel dimer conformations, and EC1–EC4 are sufficient for calcium-dependent *trans*-binding. This study provides insight into the structure and binding mechanism of CELSR cadherins and their functional implication.

Materials and Methods

DNA Construction. The plasmid encoding human CELSR2 (Kazusa DNA Research Institute: KIAA0279) was purchased from Promega, and the native signal sequence of human CELSR2 was replaced with a signal sequence of CD8. mGFP [monomeric green fluorescence protein; A206K mutation was introduced into pEGFP-N1 (Clontech)] or Halo (encoded in pFN21A; Cat# G282A; Promega) tag was fused on the C-terminal side of the plasmid and cloned into pEGFP-N1 purchased from Clontech (original EGFP portion of pEGFP-N1 was eliminated). The expression plasmid designated SP(CD8)-CELSR2-mGFP or SP(CD8)-CELSR2-Halo was transfected into CHO-K1 cells for fluorescence microscopy and cell aggregation assay. The 5′-terminal sequence of SP(CD8)-CELSR2-mGFP or SP(CD8)-CELSR2-Halo was 5′-ATGGCCTTACCAGTGACCGCCTTGTCTGCTGCCGTAGCCTTG CTGCTCCAGCCGCCA GGCCGGATTACGCGTCTTACCGTATGACGTCCAGATTACGCATCGCTGGGAGGCCCTT CGAGACCGGTCCAATTGaccgaagtggggccctgtgcttctgg...-3′ (upper letter represents the signal sequence and linker. Lower letter represents CELSR2. The latter part of CELSR2 was omitted, but identical to NCBI Reference Sequence: NM_001408.3).

To express human CELSR2 ectodomains in HEK293T cells for protein purification, the expression plasmid pcDNA3.1/V5-His A (Cat# V810-20; ThermoFisher Scientific) was used. A DNA fragment encoding signal sequence of CD8 followed

by 32 to 2378 of the amino acid region of human CELSR2, a putative extracellular region (UniProtKB/Swiss-Prot: Q9HCU4), was amplified from SP(CD8)-CELSR2-mGFP by PCR using a forward primer (5′-ATGGCCTTACCAGTGACC-3′) and a reverse primer (5′-TGTCTTACAGTGGCAGGATCTC-3′). The membrane-proximal C-terminal amino acid of the putative extracellular region was determined by domain prediction using InterPro for DNA construction (57). A DNA fragment encoding pcDNA3.1/V5-His A was amplified by PCR using a forward primer (5′-CTGCCACTGAAGACATCTAGAGGGCCCTCGAAG-3′) and a reverse primer (5′-CACTGGTAAGGCCATGAATCCACCACACTGGAC-3′). The DNA fragments of CELSR2 and pcDNA3.1/V5-His A were fused using the In-Fusion HD Cloning Kit (Cat# 639633; Takara Bio) and designated as pcDNA-SP(CD8)-CELSR2-EX-full-V5-His (EX-full), which contained V5 and His tag sequences on the C-terminal side. The pcDNA-SP(CD8)-CELSR2-EX-full-V5-His was used as a template for deletion constructs, as shown in *SI Appendix, Table S1*. The border of each cadherin ectodomain for deletion constructs was decided by XPXF/L motif, which marks the beginning of the cadherin ectodomain (58). Two fragments from the amplification of each construct, listed in *SI Appendix, Table S1*, were fused using the In-Fusion HD Cloning Kit. All constructs had a V5-His tag sequence on the C-terminal side.

Cell Culture and Fluorescence Microscopy. The CHO-K1 cells (59) were cultured at 37 °C in 5% CO₂ in Ham's F12 medium (Cat# N6658-500ML; Sigma-Aldrich) supplemented with 10% fetal bovine serum (Cat# 10270-106; ThermoFisher Scientific), 100 units/ml penicillin, and 0.1 mg/ml streptomycin (Cat# 168-23191; Fujifilm Wako Pure Chemical). SP(CD8)-CELSR2-mGFP or SP(CD8)-CELSR2-Halo was transfected using 4D-Nucleofector (Cat# AAF-1003B and AAF-1003X; Lonza) according to the manufacturer's instructions. After approximately 24 h incubation, the transfected cells were seeded on a glass-based dish (Cat# 3911-035; Iwaki). Then after incubation for another approximately 24 h, the culture medium was supplemented with 1 M calcium chloride solution (final concentration 1.8 mM) to induce CELSR2-mediated cell–cell adhesion. The cells were incubated with 5 nM HaloTag SaraFluor 650T ligand (Cat# A308-01; Goryo Chemical) or 5 nM HaloTag TMR ligand (Cat# G8252; Promega) for 1 h to label the Halo protein with fluorescent dye. The HaloTag TMR ligand was only used for the experiment as shown in Fig. 1B. Before the experiments, the cells were rinsed with the observation buffer [Hbss buffered with 10 mM Hepes (pH 7.4) containing 3 mM calcium ions] three times.

Simultaneous observations of CELSR2-mGFP and CELSR2-Halo at the single-molecule level were performed by the objective-lens-type total internal reflection (TIR) system on an inverted microscope (IX-81; Olympus) equipped with a 100× objective lens (numerical aperture (NA) 1.49; UAPON100XOTIRF; Olympus) (59, 60). To observe the cell–cell interface being formed at less than a few hundred nanometers above the glass surface, the incident angle of the laser was adjusted, which differs slightly from the TIR angle (the cell–cell interface is formed between the two plasma membranes where two facing cells are layered. Owing to the thickness of the lower cell, this interface is located slightly above the glass surface). However, even under this condition, an illumination depth is quite shallow, almost eradicating the background fluorescence that originated from the observation buffer and cytosol, allowing for identification of the single fluorescent molecules with a high signal-to-noise ratio. To capture the faint fluorescent signal emitted from the single fluorescent molecule, a two-stage microchannel plate intensifier (C8600-03; Hamamatsu Photonics) was lens-coupled with a complementary metal–oxide–semiconductor (CMOS) camera (C11440-22CU; Hamamatsu Photonics), which was operated at 30 Hz. All the observations were conducted at 37 °C. The 16-bit video image data were directly transferred to a solid-state drive in a personal computer in real time. For dual-color observation, the chromatically separated fluorescence was captured by the same two camera systems described above, and the images were overlaid according to the reported method (61). After the observation, analysis was performed using Fiji v1.5 software (NIH) (62). In particular, particle tracking was performed using the TrackMate macro in Fiji (63). More detailed information about the fluorescence data analysis is described in *SI Appendix, SI Text*.

Cell Aggregation Assay. Cell aggregation assay was modified using methods reported in previous studies (64–66). Briefly, suspended cells in Ca- and Mg-free Puck's balanced salt buffer were seeded in a 24-well plate at 5 × 10⁵ copy/ml concentration. Cells were incubated in a gyratory shaker at 80 rpm for 45 min at 37 °C in the presence or absence of 1.5 mM CaCl₂. Cell aggregates were observed using an inverted microscope (IX-70; Olympus) fitted with a 10× objective lens (NA 0.4;

UPLXAP010×; Olympus). The images that passed through a 2.5× intermediate lens were projected to Andor Clara DR-328G (Oxford Instruments) for recording.

Cell Culture and Protein Purification. HEK293T cells (gifted from Sae Tanaka) were cultured at 37 °C in 5% CO₂ in Dulbecco's Modified Eagle Medium (DMEM) (Cat# 10569010; ThermoFisher Scientific) supplemented with 10% heat-inactivated fetal bovine serum (Cat# 10569010; MP Biomedical). All transfections for protein purification were performed using the TransIT-LT1 Transfection Reagent (Cat# MIR2300; Mirus Bio) following the manufacturer's instructions. Approximately 16 h before transfection, HEK293T cells were seeded at a density of 3×10^5 /mL in 10 mL of medium in a 100-mm dish (Cat# TR4002; Nippon Genetics). Fifteen micrograms of plasmid DNA was used for each transfection. After 3 d of incubation, the conditioned medium containing secreted V5-His-tagged proteins was collected. The conditioned medium was centrifuged at $2,600 \times g$ for 5 min at 25 °C to obtain 9 mL of supernatant, which was passed through a 0.22- μ m pore-size filter (Cat# SLGPR33RS; Merck KGaA). AV5-tagged protein magnetic purification kit (Cat# 3341; Medical & Biological Laboratories) was used according to the manufacturer's instructions to purify V5-His-tagged proteins from the supernatants. The purified proteins were stored in PBS containing 1 mM CaCl₂ at 4 °C or –80 °C until further use. The purified proteins were separated on a 12.5% polyacrylamide gel (Cat# 199-14971; Fujifilm Wako Pure Chemical) and analyzed by Coomassie brilliant blue staining (*SI Appendix, Fig. S6*).

Analysis of N-Terminal Amino Acid Sequence. The purified protein (~15 μ g; ~0.2 nmol) was subjected to electrophoresis in 4 to 20% SDS-PAGE and transferred to a polyvinylidene difluoride membrane. The membrane was stained with 0.1% Coomassie Brilliant Blue R-250 in 10% methanol–7% acetic acid. The protein band to be analyzed was cut out and washed with 50% methanol, and then sequenced by automated Edman degradation using a Shimadzu PPSQ-33A instrument (Shimadzu).

Bead Aggregation Assay. Two microliters of anti-His-tagged magnetic beads (Cat# D291-11; Medical & Biological Laboratories) and 2 μ L of purified V5-His-tagged protein solution were mixed in a 1.5-mL tube and incubated for 15 min at 25 °C. The bead suspensions were diluted in 1 mL HKNC (10 mM Hepes, 5 mM KCl, 140 mM NaCl, 2 mM CaCl₂, pH 7.4) or HKNE [10 mM Hepes (pH 7.4), 5 mM KCl, 140 mM NaCl, and 10 mMethylene glycol-bis(β -aminoethyl ether)-N,N,N',N'-tetraacetic acid (EGTA)] buffer and transferred to a 12-well suspension culture plate (Cat#665102; Greiner Bio-One). Before the addition of bead suspensions, the suspension culture plate was coated with bovine serum albumin (2 μ g/mL) to avoid nonspecific binding of bead to the bottom of the plate and washed by HKN (10 mM Hepes, 5 mM KCl, 140 mM NaCl, pH 7.4) buffer. Following the addition of diluted bead suspensions, the plate was stored for 10 min, followed by a 10 min rotation at 180 rpm on a horizontal shaker (MMS-3010; Tokyo Rikakikai) at 25 °C. The plate was kept still for 10 min to allow the beads to settle onto the bottom, and then slowly moved to the stage of an inverted microscope (IX73; Olympus). Images of bead distribution were captured to obtain a single image (1,920 \times 1,080 pixels) in four different areas for each well using a 20× objective lens and a digital color camera (DP74; Olympus). The images were trimmed to 1,080 \times 1,080 pixels, and the contrast was adjusted using ImageJ 1.51d software (NIH) (62). The average size of bead aggregation was calculated using Analyze Particles of ImageJ. Two or more independent protein purifications and bead aggregation assays were performed for each recombinant protein. All images of bead aggregation assay obtained in this study were deposited in the Mendeley Data Repository (67).

Protein Preparation for HS-AFM. A mica substrate with a diameter of 1.5 mm and a thickness of 0.1 mm (Furuuchi Chemical) was attached with glue on a glass stage. A 2- μ L droplet of 0.03 to 0.04% 3-aminopropyltriethoxysilane (APTES) solution was placed on a freshly cleaved mica substrate and incubated for 3 min.

The APTES-mica substrate was then washed twice with 80 μ L Milli-Q water. A 2- μ L droplet of purified protein solution was placed on the APTES-mica substrate for 3 min and washed with 80 μ L HKNC buffer. HS-AFM in EGTA-containing buffer was performed using HKNE instead of HKNC buffer. For LAFM analysis, the adsorption of purified proteins on mica substrate was performed using 0.1% APTES, and a 2- μ L droplet of 2% glutaraldehyde was placed on the APTES-mica substrate for 3 min after the adsorption of purified proteins and washed with 80 μ L HKNC buffer. The concentration of purified proteins for adsorption was adjusted based on the pilot observations.

HS-AFM. HS-AFM observations were carried out with a laboratory-made instrument at room temperature (25 °C) in HKNC buffer (68). As an AFM cantilever, we used a miniaturized cantilever made by Olympus (BL-AC10DS-A2: 9 μ m length, a width of 2 μ m, and a thickness of 0.13 μ m) with a spring constant of approximately 0.1 Nm⁻¹, resonant frequencies around 500 kHz, and a Q value below 1 in an aqueous environment. The sharp probes of the AFM are made of carbon pillars formed by the so-called electric beam deposition method using a single point of electron beam irradiation with a scanning electron microscope. In addition, carbon pillars are sharpened to a tip radius of 2 to 5 nm by plasma etching with argon gas (69). The HS-AFM is operated in tapping mode, so the cantilever oscillates with a free oscillation amplitude of 1 to 2 nm near the resonance frequency. Feedback control for the HS-AFM imaging was performed with the cantilever oscillation reduced to approximately 80% of its free amplitude. Two or more independent protein purifications and HS-AFM measurements were performed on all samples. All raw data used in this study are deposited in the Mendeley Data Repository (67).

HS-AFM Image Processing and Analysis. HS-AFM image processing was performed using the laboratory-made analysis software FalconViewer based on Igor Pro-8 (WaveMetrics). The angle of the hinge region of monomers and the length of the major axis of dimers of CELSR cadherin were measured using ImageJ 1.51d software (NIH) (62). The angle distributions from sequential images of the monomers were measured using up to 127 frames of HS-AFM images in each dimer of the six EX-full dimers (Fig. 3 B–D and *SI Appendix, Fig. S9*). For the LAFM analysis of EC1-8 dimers, we manually adjusted the center position of sequential 28 to 112 HS-AFM images of single dimers (Fig. 5 D and E). We generated a single LAFM image composed of local maxima of the sequential HS-AFM images using the ImageJ plugin previously released by Heath et al. (47). To extract local maxima with higher spatial precision, pixels (0.5 nm/pixel) of raw HS-AFM images were expanded four times using bicubic interpolation on ImageJ before the input of HS-AFM images to LAFM plugin. The numerical data obtained in this study are deposited in the Mendeley Data Repository (67).

Data, Materials, and Software Availability. Image files data have been deposited in Mendeley Data (10.17632/vbpdtyxbtn.3) (67). All study data are included in the article and/or *SI Appendix*.

ACKNOWLEDGMENTS. This work was supported by the Grant-in-Aid for Early-Career Scientists JP 22K14577 (to S.N.) and Grant-in-Aid for Scientific Research JP 17K07333, JP 18H05269, JP 18H05424, and JP 20H03225 (to R.S.K.); JP 21H00393, JP 21H01772, and JP 22K18943 (to T.U.) from Japan Society for the Promotion of Science; and by the Joint Research of the Exploratory Research Center on Life and Living Systems: Program 18-101 (to T.U.) and Program 22EXC312 (to R.S.K.).

Author affiliations: ^aExploratory Research Center on Life and Living Systems, National Institutes of Natural Sciences, Okazaki 444-8787, Japan; ^bInstitute for Life and Medical Sciences, Kyoto University, Kyoto 606-8507, Japan; ^cInstitute for Glyco-core Research, Gifu University, Gifu 501-1193, Japan; ^dDepartment of Physics, Nagoya University, Nagoya 464-8602, Japan; and ^eInstitute for Glyco-core Research, Nagoya University, Nagoya 464-8602, Japan

1. J. Brasch, O. J. Harrison, B. Honig, L. Shapiro, Thinking outside the cell: How cadherins drive adhesion. *Trends Cell Biol.* **22**, 299–310 (2012).
2. M. Takeichi, Dynamic contacts: Rearranging adherens junctions to drive epithelial remodeling. *Nat. Rev. Mol. Cell Biol.* **15**, 397–410 (2014).
3. G. Bex, F. van Roy, Involvement of members of the cadherin superfamily in cancer. *Cold Spring Harb. Perspect. Biol.* **1**, a003129–a003129 (2009).

4. T. J. C. Harris, U. Tepass, Adherens junctions: From molecules to morphogenesis. *Nat. Rev. Mol. Cell Biol.* **11**, 502–514 (2010).
5. R. Fernandez-Gonzalez, M. Peifer, Powering morphogenesis: Multiscale challenges at the interface of cell adhesion and the cytoskeleton. *Mol. Biol. Cell* **33**, pe4 (2022).
6. P. Hulpiau, F. van Roy, Molecular evolution of the cadherin superfamily. *Int. J. Biochem. Cell Biol.* **41**, 349–369 (2009).

7. T. J. Boggon, C-cadherin ectodomain structure and implications for cell adhesion mechanisms. *Science* **296**, 1308–1313 (2002).
8. D. Häußinger *et al.*, Proteolytic E-cadherin activation followed by solution NMR and X-ray crystallography. *EMBO J.* **23**, 1699–1708 (2004).
9. E. Parisini, J. M. G. Higgins, J. Liu, M. B. Brenner, J. Wang, The crystal structure of human E-cadherin domains 1 and 2, and comparison with other cadherins in the context of adhesion mechanism. *J. Mol. Biol.* **373**, 401–411 (2007).
10. L. Shapiro *et al.*, Structural basis of cell-cell adhesion by cadherins. *Nature* **374**, 327–337 (1995).
11. S. D. Patel *et al.*, Type II cadherin ectodomain structures: Implications for classical cadherin specificity. *Cell* **124**, 1255–1268 (2006).
12. M. Sotomayor, K. Schulten, The allosteric role of the Ca²⁺ switch in adhesion and elasticity of C-cadherin. *Biophys. J.* **94**, 4621–4633 (2008).
13. J. Vendome *et al.*, Molecular design principles underlying β strand swapping in the adhesive dimerization of cadherins. *Nat. Struct. Mol. Biol.* **18**, 693–700 (2011).
14. D. Häußinger *et al.*, Calcium-dependent homoassociation of E-cadherin by NMR spectroscopy: Changes in mobility, conformation and mapping of contact regions. *J. Mol. Biol.* **324**, 823–839 (2002).
15. D. Modak, M. Sotomayor, Identification of an adhesive interface for the non-clustered δ 1 protocadherin-1 involved in respiratory diseases. *Commun. Biol.* **2**, 354 (2019).
16. J. Brasch *et al.*, Visualization of clustered protocadherin neuronal self-recognition complexes. *Nature* **569**, 280–283 (2019).
17. K. Sano *et al.*, Protocadherins: A large family of cadherin-related molecules in central nervous system. *EMBO J.* **12**, 2249–2256 (1993).
18. D. Canzio, T. Maniatis, The generation of a protocadherin cell-surface recognition code for neural circuit assembly. *Curr. Opin. Neurobiol.* **59**, 213–220 (2019).
19. O. J. Harrison *et al.*, Family-wide structural and biophysical analysis of binding interactions among non-clustered δ -protocadherins. *Cell Rep.* **30**, 2655–2671.e7 (2020).
20. G. Dionne *et al.*, Mechanotransduction by PCDH15 relies on a novel cis-dimeric architecture. *Neuron* **99**, 480–492.e5 (2018).
21. P. Kazmierczak *et al.*, Cadherin 23 and protocadherin 15 interact to form tip-link filaments in sensory hair cells. *Nature* **449**, 87–91 (2007).
22. M. Sotomayor, W. A. Weihofen, R. Gaudet, D. P. Corey, Structure of a force-conveying cadherin bond essential for inner-ear mechanotransduction. *Nature* **492**, 128–132 (2012).
23. J. Elferich *et al.*, Molecular structures and conformations of protocadherin-15 and its complexes on stereocilia elucidated by cryo-electron tomography. *Elife* **10**, e74512 (2021).
24. X. Qiu, U. Müller, Sensing sound: Cellular specializations and molecular force sensors. *Neuron* **110**, 3667–3687 (2022).
25. B. Kachar, M. Parakkal, M. Kurc, Y. Zhao, P. G. Gillespie, High-resolution structure of hair-cell tip links. *Proc. Natl. Acad. Sci. U.S.A.* **97**, 13336–13341 (2000).
26. Y. Tsukasaki *et al.*, Giant cadherins fat and dachsous self-bend to organize properly spaced intercellular junctions. *Proc. Natl. Acad. Sci. U.S.A.* **111**, 16011–16016 (2014).
27. I. S. Gul, P. Hulpliau, Y. Saeyes, F. van Roy, Evolution and diversity of cadherins and catenins. *Exp. Cell Res.* **358**, 3–9 (2017).
28. A.-K. Hadjantonakis, C. J. Formstone, P. F. R. Little, MCelsr1 is an evolutionarily conserved seven-pass transmembrane receptor and is expressed during mouse embryonic development. *Mech. Dev.* **78**, 91–95 (1998).
29. M. Nakayama *et al.*, Identification of high-molecular-weight proteins with multiple EGF-like motifs by motif-trap screening. *Genomics* **51**, 27–34 (1998).
30. T. Usui *et al.*, Flamingo, a seven-pass transmembrane cadherin, regulates planar cell polarity under the control of frizzled. *Cell* **98**, 585–595 (1999).
31. J. Chae *et al.*, The drosophila tissue polarity gene *starry night* encodes a member of the protocadherin family. *Development* **126**, 5421–5429 (1999).
32. D. Shi, M. Arata, T. Usui, T. Fujimori, T. Uemura, “Seven-pass transmembrane cadherin CELSRs, and Fat4 and Dchs1 cadherins: From planar cell polarity to three-dimensional organ architecture” in *The Cadherin Superfamily*, S. T. Suzuki, S. Hirano, Eds. (Springer Tokyo, 2016), pp. 251–275.
33. S. Yona, H.-H. Lin, W. O. Siu, S. Gordon, M. Stacey, Adhesion-GPCRs: Emerging roles for novel receptors. *Trends Biochem. Sci.* **33**, 491–500 (2008).
34. C. Boutin, A. M. Goffinet, F. Tissir, Celsr1–3 cadherins in PCP and brain development. *Curr. Top Dev. Biol.* **101**, 161–183 (2012).
35. Y. Shima *et al.*, Differential expression of the seven-pass transmembrane cadherin genes *Celsr1–3* and distribution of the *Celsr2* protein during mouse development. *Dev. Dyn.* **223**, 321–332 (2002).
36. J. A. Curtin *et al.*, Mutation of *Celsr1* disrupts planar polarity of inner ear hair cells and causes severe neural tube defects in the mouse. *Curr. Biol.* **13**, 1129–1133 (2003).
37. D. Devenport, E. Fuchs, Planar polarization in embryonic epidermis orchestrates global asymmetric morphogenesis of hair follicles. *Nat. Cell Biol.* **10**, 1257–1268 (2008).
38. F. Tissir *et al.*, Lack of cadherins *Celsr2* and *Celsr3* impairs ependymal gliogenesis, leading to fatal hydrocephalus. *Nat. Neurosci.* **13**, 700–707 (2010).
39. S. N. Stahley, L. P. Basta, R. Sharan, D. Devenport, Celsr1 adhesive interactions mediate the asymmetric organization of planar polarity complexes. *Elife* **10** (2021).
40. Y. Shima, M. Kengaku, T. Hirano, M. Takeichi, T. Uemura, Regulation of dendritic maintenance and growth by a mammalian 7-pass transmembrane cadherin. *Dev. Cell* **7**, 205–216 (2004).
41. X.-J. Wang *et al.*, Understanding cadherin EGF LAG seven-pass G-type receptors. *J. Neurochem.* **131**, 699–711 (2014).
42. R. S. Kasai *et al.*, Full characterization of GPCR monomer–dimer dynamic equilibrium by single molecule imaging. *J. Cell Biol.* **192**, 463–480 (2011).
43. R. S. Kasai *et al.*, Metastable GPCR dimers trigger the basal signal by recruiting G-proteins (2020). 10.1101/2020.02.10.929588. Accessed 16 March 2023.
44. O. J. Harrison *et al.*, The extracellular architecture of adherens junctions revealed by crystal structures of type I cadherins. *Structure* **19**, 244–256 (2011).
45. M. R. Emond, J. D. Jontes, Bead aggregation assays for the characterization of putative cell adhesion molecules. *J. Vis. Exp.* **92**, e51762 (2014). 10.3791/51762.
46. J. Vesenka, S. Manne, R. Giberson, T. Marsh, E. Henderson, Colloidal gold particles as an incompressible atomic force microscope imaging standard for assessing the compressibility of biomolecules. *Biophys. J.* **65**, 992–997 (1993).
47. G. R. Heath *et al.*, Localization atomic force microscopy. *Nature* **594**, 385–390 (2021).
48. R. B. Troyanovsky, O. Laur, S. M. Troyanovsky, Stable and unstable cadherin dimers: Mechanisms of formation and roles in cell adhesion. *Mol. Biol. Cell* **18**, 4343–4352 (2007).
49. Y. Zhang, S. Sivasankar, W. J. Nelson, S. Chu, Resolving cadherin interactions and binding cooperativity at the single-molecule level. *Proc. Natl. Acad. Sci. U.S.A.* **106**, 109–114 (2009).
50. X. Jin *et al.*, Crystal structures of drosophila N-cadherin ectodomain regions reveal a widely used class of Ca²⁺-free interdomain linkers. *Proc. Natl. Acad. Sci. U.S.A.* **109**, E127–E134 (2012).
51. S. Nishiguchi, H. Oda, Structural variability and dynamics in the ectodomain of an ancestral-type classical cadherin revealed by AFM imaging. *J. Cell Sci.* **134**, jcs258388 (2021).
52. M. Sikora *et al.*, Desmosome architecture derived from molecular dynamics simulations and cryo-electron tomography. *Proc. Natl. Acad. Sci. U.S.A.* **117**, 27132–27140 (2020).
53. S. Nishiguchi, T. Furuta, T. Uchihashi, Multiple dimeric structures and strand-swap dimerization of E-cadherin in solution visualized by high-speed atomic force microscopy. *Proc. Natl. Acad. Sci. U.S.A.* **119**, e2208067119 (2022).
54. Q. Chen, R. Takada, C. Noda, S. Kobayashi, S. Takada, Different populations of Wnt-containing vesicles are individually released from polarized epithelial cells. *Sci. Rep.* **6**, 35562 (2016).
55. J. C. Gross, V. Chaudhary, K. Bartscherer, M. Boutos, Active Wnt proteins are secreted on exosomes. *Nat. Cell Biol.* **14**, 1036–1045 (2012).
56. R. Kalluri, V. S. LeBleu, The biology, function, and biomedical applications of exosomes. *Science* **367**, eaau6977 (2020).
57. M. Blum *et al.*, The InterPro protein families and domains database: 20 years on. *Nucleic Acids Res.* **49**, D344–D354 (2021).
58. S. Posy, L. Shapiro, B. Honig, Sequence and structural determinants of strand swapping in cadherin domains: Do all cadherins bind through the same adhesive interface? *J. Mol. Biol.* **378**, 954–968 (2008).
59. R. S. Kasai, S. V. Ito, R. M. Awane, T. K. Fujiwara, A. Kusumi, The class-A GPCR dopamine D2 receptor forms transient dimers stabilized by agonists: Detection by single-molecule tracking. *Cell Biochem. Biophys.* **76**, 29–37 (2018).
60. R. Nagai *et al.*, Functional reconstitution of dopamine D2 receptor into a supported model membrane in a nanometric confinement. *Adv. Biol.* **5**, 2100636 (2021).
61. I. Koyama-Honda *et al.*, Fluorescence imaging for monitoring the colocalization of two single molecules in living cells. *Biophys. J.* **88**, 2126–2136 (2005).
62. J. Schindelin *et al.*, Fiji: An open-source platform for biological-image analysis. *Nat. Methods* **9**, 676–682 (2012).
63. D. Ershov *et al.*, TrackMate 7: Integrating state-of-the-art segmentation algorithms into tracking pipelines. *Nat. Methods* **19**, 829–832 (2022).
64. A. Nagafuchi, Y. Shirayoshi, K. Okazaki, K. Yasuda, M. Takeichi, Transformation of cell adhesion properties by exogenously introduced E-cadherin cDNA. *Nature* **329**, 341–343 (1987).
65. A. Nagafuchi, M. Takeichi, Cell binding function of E-cadherin is regulated by the cytoplasmic domain. *EMBO J.* **7**, 3679–3684 (1988).
66. H. Urushihara, H. S. Ozaki, M. Takeichi, Immunological detection of cell surface components related with aggregation of chinese hamster and chick embryonic cells. *Dev. Biol.* **70**, 206–216 (1979).
67. S. Nishiguchi, R. S. Kasai, T. Uchihashi, Data for: Antiparallel dimer structure of CELSR cadherin in solution revealed by high-speed atomic force microscopy. Mendeley data. <https://data.mendeley.com/datasets/vbpdtyxbtn/3>. Deposited 21 March 2023.
68. T. Ando *et al.*, A high-speed atomic force microscope for studying biological macromolecules. *Proc. Natl. Acad. Sci. U.S.A.* **98**, 12468–12472 (2001).
69. M. Wendel, H. Lorenz, J. P. Kotthaus, Sharpened electron beam deposited tips for high resolution atomic force microscope lithography and imaging. *Appl. Phys. Lett.* **67**, 3732–3734 (1995).